Supporting Information

Activated and nitrogen-doped exfoliated graphene as air electrodes for metal-air battery applications

Drew Higgins‡, Zhu Chen‡, Dong Un Lee and Zhongwei Chen[*]

Department of Chemical Engineering

Waterloo Institute for Nanotechnology

Waterloo Institute for Sustainable Energy

University of Waterloo

Waterloo, ON, Canada, N2L 3G1

*Corresponding Author

Email: zhwchen@uwaterloo.ca,

Telephone: 1-519-888-4567 Ext. 38664,

Fax: 1-519-746-4979

‡Indicates joint first authorship.

1.0 Physicochemical characterization

1.1 SEM

SEM images of the samples were obtained throughout all stages of N-a-ex-G synthesis and are provided in Figure S1. The SEM image of GO (Figure S1a) displays a layered structure consisting of several stacked sheets of GO, with low surface areas that are not desirable for successful nitrogen precursor penetration and high surface area catalysis. In contrast, the SEM image of ex-G (Figure S1b) demonstrates a voile-like structure, with clear indication of graphene sheet separation. This is due to exothermic decomposition of oxygen containing species that result in gaseous species emission and in immense pressure buildup between the graphene sheets providing a high degree of exfoliation.[1] a-ex-G (Figure S1c) and N-a-ex-G (Figure S1d) show well exfoliated voile-like structures, with reduced sheet agglomeration in comparison to ex-G. Moreover, a significant increase in the number of folds is observed for a-ex-G and N-a-ex-G samples. For the latter case with a higher degree of folding apparent, this could be due to the introduction of nitrogen defects into the graphene lattice.

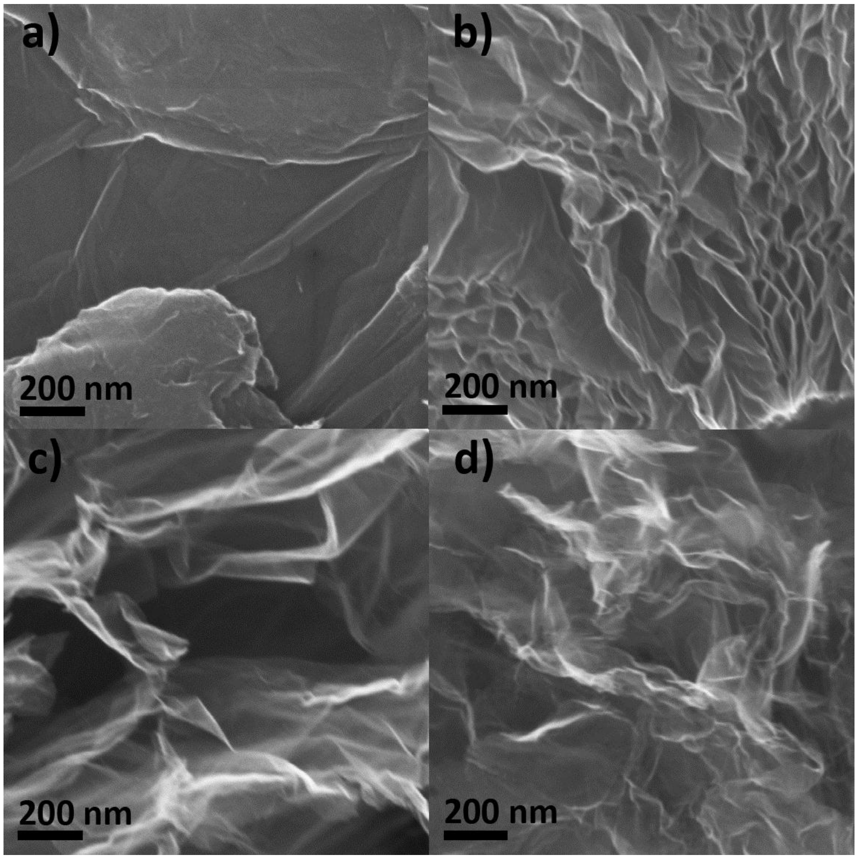

Figure S1. SEM image of a) GO, b) ex-G, c) a-ex-G and d) N-a-ex-G

1.2 BET surface area analysis

BET surface area analysis was utilized in order to evaluate the surface area of the synthesized N-a-ex-G catalyst. The BET adsorption isotherm is provided in Figure S2, with the apparent surface area determined to be 2980 m^2g^{-1}. In particular, a Type IV adsorption isotherm was demonstrated along with a type H3 hysteresis loop. These features indicated the presence of a large number of micro and macropores, the latter possessing a slit-like structure and most likely attributed to the pores between individual graphene sheets. This exemplary surface area can be directly attributed to the activation procedure carried out prior to nitrogen doping that has been deemed capable of providing BET surface areas higher than the theoretical surface area of pristine graphene,[2] and in the present study provided surface areas almost 5 times higher than those previously reported for nitrogen-doped graphene materials.[3, 4] This dramatic improvement will provide essential benefits for catalysis and other applications that depend on high surface areas for performance improvement.

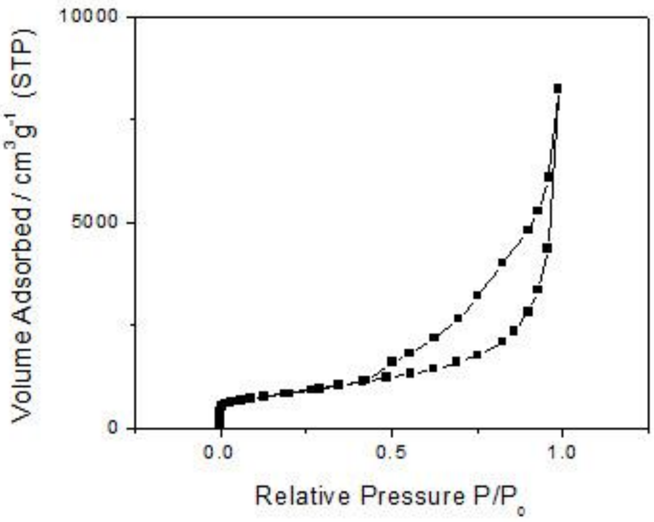

Figure S2. BET adsorption isotherm of N-a-ex-G

1.3 X-ray photoelectron spectroscopy

High resolution C1s signals from XPS analysis are provided in Figure S3. From analysis of the GO (Figure S3a) and ex-G (Figure S3b) profile, clear suppression of the C-O species peaks from ca. 286-290 eV[5] are observed, confirming the successful reduction of oxygen containing species. Moreover, the sp^2 bonded carbon peak of ex-G at ca. 284.6 eV is sharpened, indicating an increase in the graphitic carbon configuration.[6] These results combined with the morpholofy changes observed by TEM and SEM indicate the effectiveness of the thermal exfoliation and reduction technique. Following KOH chemical activation, the oxygen content was found to decrease from 7.49 at. % for ex-G to 4.51 at. % for a-ex-G. This is a common observation for KOH activated carbons that are adequately washed.[2, 7] The broad shoulder at higher binding energies of the C1s spectra for a-ex-G (Figure S3c) and N-a-ex-G (Figure S3d), where applicable can be attributed to a combination of C-O, C-N, carbonate and potassium (most likely in the form of K_2CO_3) species along with π- π* excitation (shake up) states.

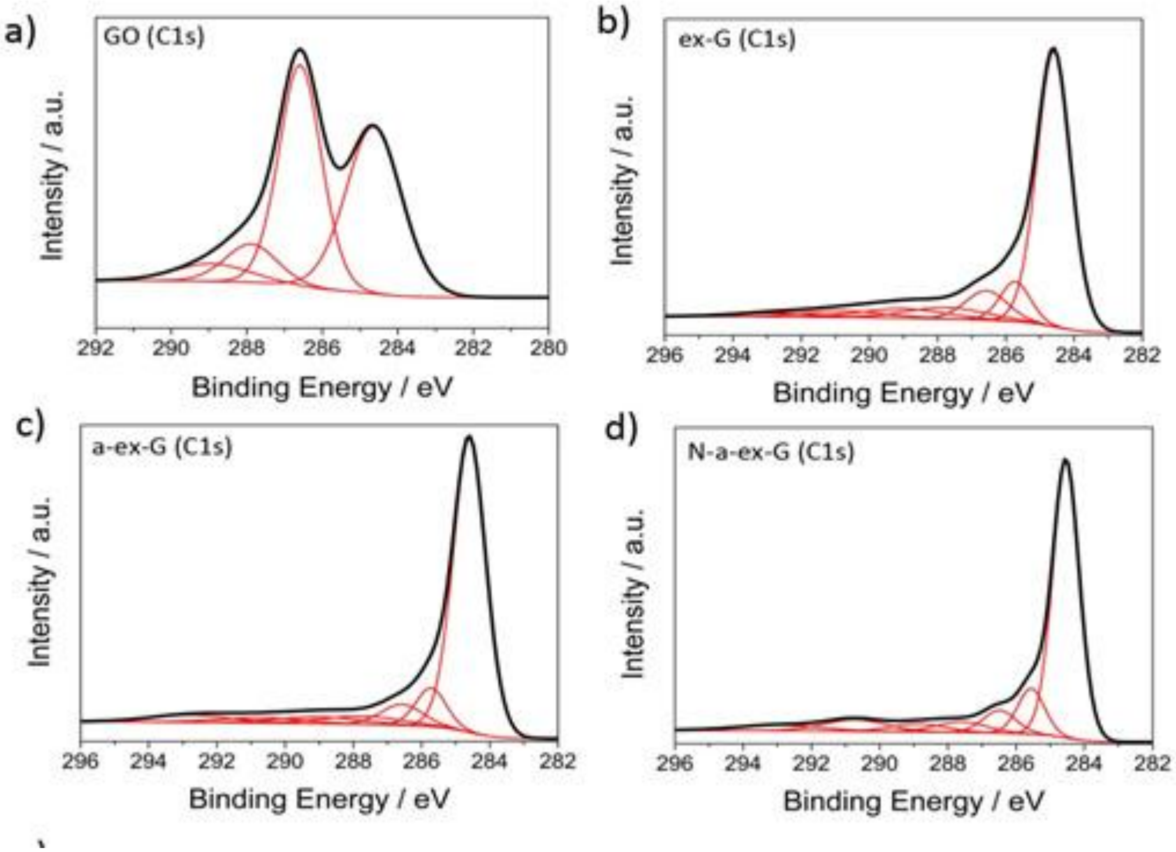

Figure S3. High resolution XPS C1s spectra for a) GO, b) ex-G, c) a-ex-G and d) N-a-ex-G.

1.4 X-ray diffraction study

XRD patterns of GO and N-a-ex-G are provided in Figure S4. For GO, a sharp diffraction peak is observed at a 2-theta diffraction angle of approximately 11^o. This peak is observed due to the intercalation of oxygen functional groups in between the individual graphene sheets resulting in increased d-spacing.[8, 9] N-a-ex-G conversely displayed the common (002) diffraction peak for graphene materials at a 2-theta diffraction angle of approximately 26^o. This peak indicates a decrease in the d-spacing of the N-a-ex-G, and the peak broadness is indicative of the disorder present in the samples[8] and smaller crystal domains attributed to the chemical activation and nitrogen incorporation as previously evidenced by Raman spectroscopy.

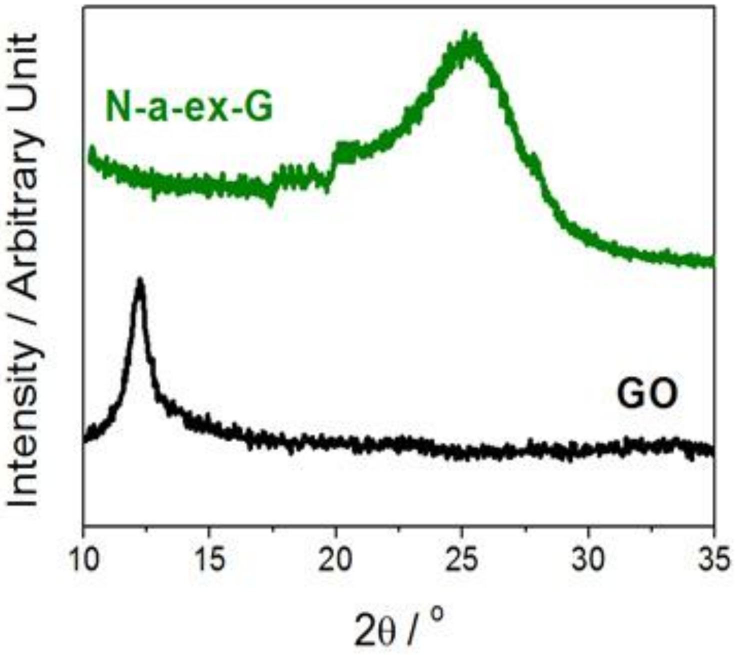

Figure S4. XRD pattern of GO and N-a-ex-G

2.0 Electrochemical characterization

Reduction of oxygen is a crucial reaction occurring at the air electrode of metal-air batteries, and the development of unique catalyst technologies with improved kinetics will provide marked performance benefits. Evaluation of catalyst ORR activity was carried out in oxygen saturated 0.1 M KOH electrolyte at electrode rotation rates of 100, 400, 900 and 1600 rpm. The full polarization plots for all catalyst samples are provided herein with the exception of GO which displayed negligible ORR activity. Furthermore, the details of Koutcky-Levich analysis applied to N-a-ex-G are described.

2.1 Koutecky-Levich analysis

The Koutecky-Levich relationship can provide analytical insight into the ORR kinetics occurring on catalyst materials and is provided in equation (1):

$$\frac{1}{i} = \frac{1}{i_k} + \frac{1}{B\omega^{-1/2}} \qquad (1)$$

In equation (1), i is the measured current density, i_k is the kinetically limited current density, ω is the electrode rotation speed, and the term $B\omega^{-1/2}$ accounts for the oxygen diffusion limited current density. The value of B can be defined by equation (2):

$$B = 0.62nF[O_2]D_{O_2}^{2/3}\upsilon^{-1/6} \quad (2)$$

In equation (2), n is the number of electrons transferred between 2 for a partial reduction to purely peroxide species, or 4 for a complete reduction to purely hydroxide species, F is Faraday's constant, $[O_2]$ is the concentration of oxygen in the electrolyte, D_{O2} is the diffusivity of oxygen in the electrolyte, and ν is the solution viscosity.

2.2 N-a-ex-G half-cell analysis

ORR polarization curves for N-a-ex-G obtained at varying electrode rotation rates are provided in Figure S5a.

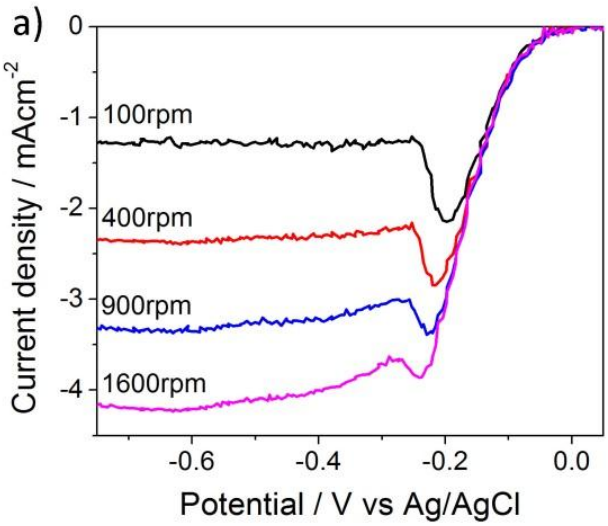

Figure S5. a) ORR polarization curves of N-a-ex-G carried out in 0.1 M KOH electrolyte saturated with oxygen at an electrode potential scan rate of 10 mVs^{-1}.

2.3 a-ex-G half-cell analysis

ORR polarization curves for a-ex-G obtained at varying electrode rotation rates are provided in Figure S6.

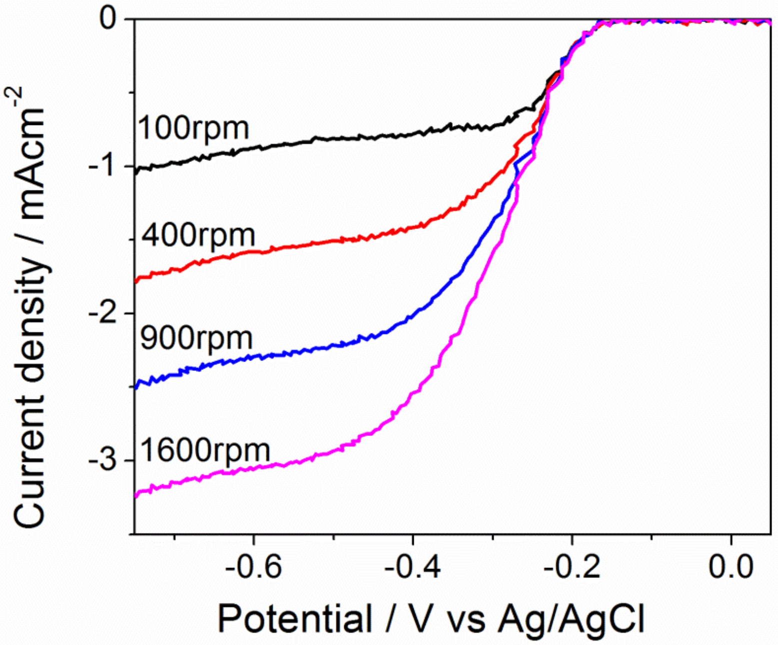

Figure S6. ORR polarization curves of a-ex-G carried out in 0.1 M KOH electrolyte saturated with oxygen at an electrode potential scan rate of 10 mVs^{-1}.

2.4 ex-G half-cell analysis

ORR polarization curves for ex-G obtained at varying electrode rotation rates are provided in Figure S7.

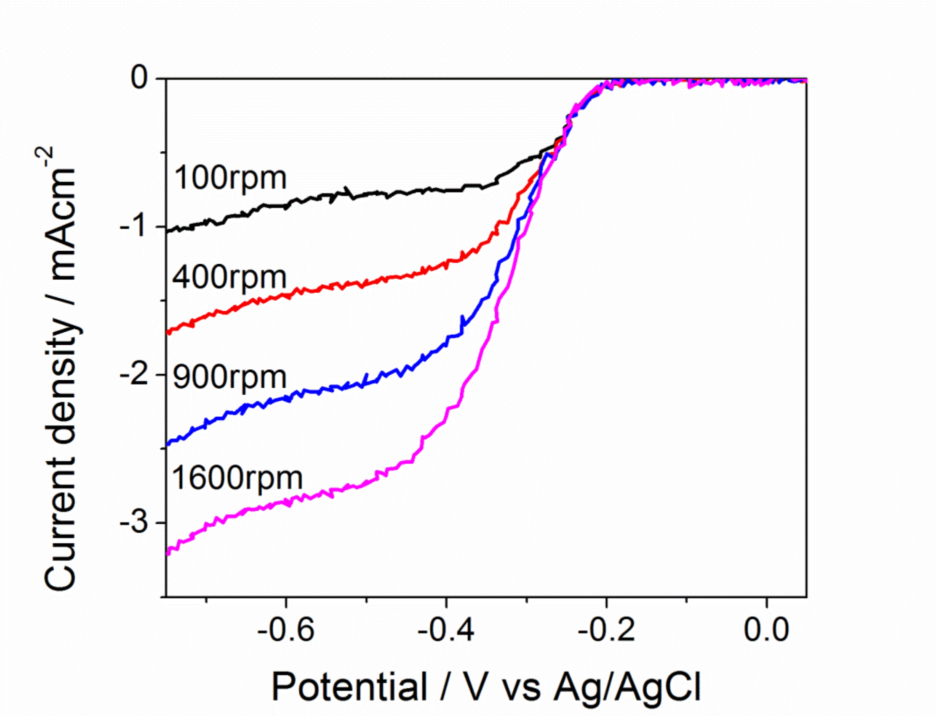

Figure S7. ORR polarization curves of ex-G carried out in 0.1 M KOH electrolyte saturated with oxygen at an electrode potential scan rate of 10 mVs^{-1}.

2.5 Pt/C half-cell analysis

ORR polarization curves for Pt/C obtained at varying electrode rotation rates are provided in Figure S8.

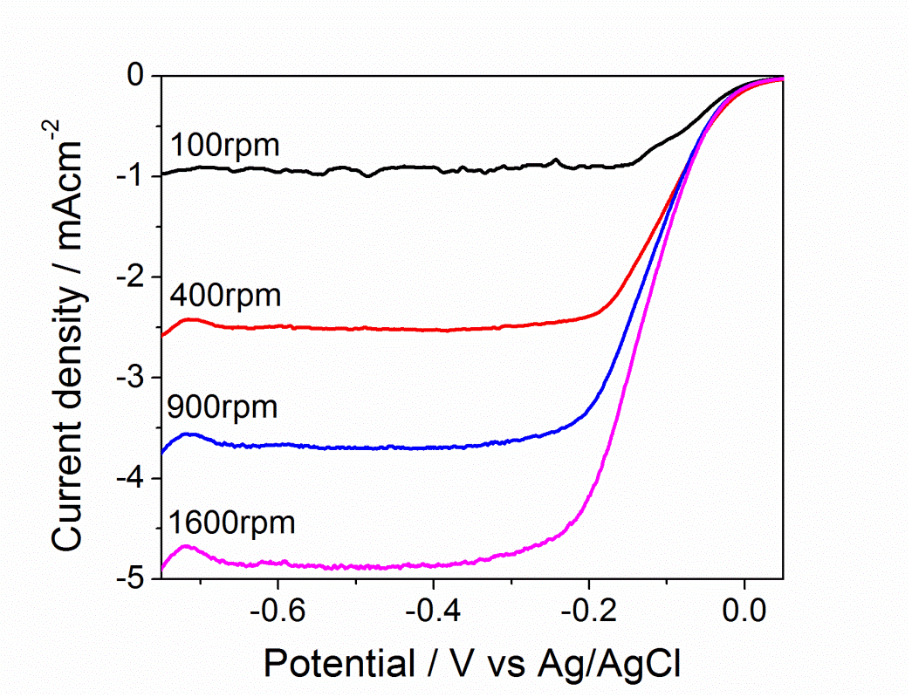

Figure S8. ORR polarization curves of commercial Pt/C carried out in 0.1 M KOH electrolyte saturated with oxygen at an electrode potential scan rate of 10 mVs^{-1}.

3.0 Practical metal-air battery performance evaluation

3.1 Zinc-air battery testing

Zinc-air battery testing using catalyst coated air electrodes was carried out using an in-house made single cell, with a schematic and picture of the cell setup provided in Figure S9a and S9b, respectively. Figure S9c highlights the zinc-air battery performance on an active electrode surface area basis.

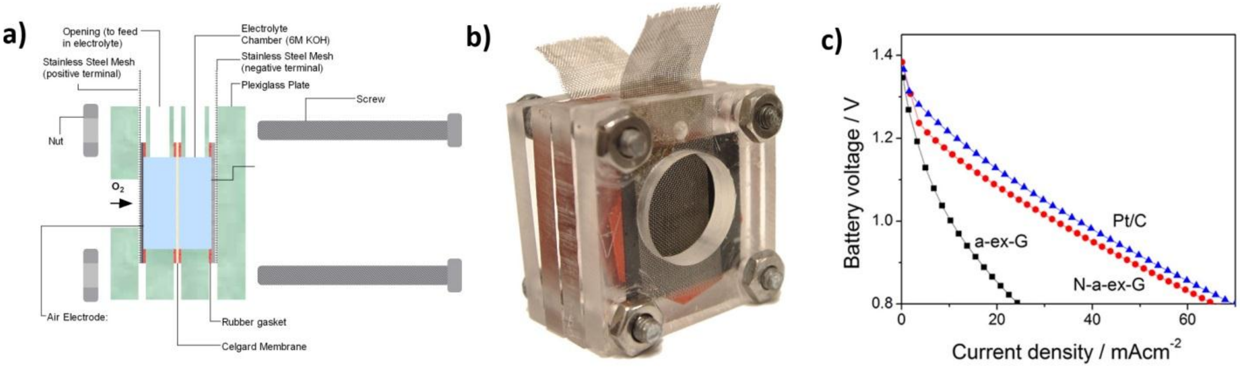

Figure S9. a) Schematic and b) picture of in-house made zinc-air cell used to evaluate air electrode discharge performance. c) Zinc-air battery polarization curve in terms of current density (active electrode surface area of 2.84 cm^2).

3.2 AC impedance spectroscopy

AC Impedance spectroscopy was performed for the different catalyst coated air electrodes. Obtained results were simulated using ZSimpWin version 3.10 and fitted to the equivalent circuit provided in the inset of Figure 5a. In the equivalent circuit, five circuit elements, R_s, Q_{int}, R_{int}, Q_{dl} and R_{ct} were used to model the impedance data. Various resistances associated with battery components, such as the electrolyte and contact resistance are represented by R_s. The resistance arising from the solid electrolyte interface is represented by R_{int}. The charge transfer resistance encountered during the electrochemical reactions on the electrodes is represented by R_{ct}. The constant phase elements, Q_{int} and Q_{dl} are incorporated into the equivalent circuit to represent the capacitances that arise from the solid electrolyte interface on the air electrode. Calculated equivalent circuit resistance values are provided in Table S1.

Table S1. Calculated equivalent circuit resistance values calculated from electrochemical impedance data fitting to the equivalent circuit provided in Figure S11.

Sample	**Rs (Ω)**	**Rint (Ω)**	**Rct (Ω)**
a-ex-G	1.567	0.220	1.746
N-a-ex-G	1.520	0.149	0.685
Pt/C	1.722	0.155	0.484

References

1 M. J. McAllister, J.-L. Li, D. H. Adamson, H. C. Schniepp, A. A. Abdala, J. Liu, M. Herrera-Alonso, D. L. Milius, R. Car, R. K. Prud'homme and I. A. Aksay, *Chem. Mater.*, 2007, **19**, 4396.
2 Y. Zhu, S. Murali, M. D. Stoller, K. J. Ganesh, W. Cai, P. J. Ferreira, A. Pirkle, R. M. Wallace, K. A. Cychosz, M. Thommes, D. Su, E. A. Stach and R. S. Ruoff, *Science*, 2011, **332**, 1537.
3 D. Geng, S. Yang, Y. Zhang, J. Yang, J. Liu, R. Li, T.-K. Sham, X. Sun, S. Ye and S. Knights, *Appl. Surf. Sci.*, 2011, **257**, 9193.
4 L. Sun, L. Wang, C. Tian, T. Tan, Y. Xie, K. Shi, M. Li and H. Fu, *RSC Adv.*, 2012, **2**, 4498.
5 C. Mattevi, G. Eda, S. Agnoli, S. Miller, K. A. Mkhoyan, O. Celik, D. Mastrogiovanni, G. Granozzi, E. Garfunkel and M. Chhowalla, *Adv. Funct. Mater.*, 2009, **19**, 2577.
6 S. Maldonado, S. Morin and K. J. Stevenson, *Carbon*, 2006, **44**, 1429.
7 J. Díaz-Terán, D. M. Nevskaia, J. L. G. Fierro, A. J. López-Peinado and A. Jerez, *Microporous Mesoporous Mater.*, 2003, **60**, 173.
8 A. Kaniyoor, T. T. Baby and S. Ramaprabhu, *J. Mater. Chem.*, 2010, **20**, 8467.
9 G. Wang, J. Yang, J. Park, X. Gou, B. Wang, H. Liu and J. Yao, *J. Phys. Chem. C*, 2008, **112**, 8192.